

Analysis of low pressure rf glow discharges using a continuum model

Sang-Kyu Park^{a)} and Demetre J. Economou^{b)}

Department of Chemical Engineering, University of Houston, Houston, Texas 77204-4792

(Received 19 April 1990; accepted for publication 26 June 1990)

A continuum model was used to analyze charged particle transport and potential distribution in low-pressure radio frequency (rf) glow discharges. The method of lines with orthogonal collocation on finite elements for the spatial discretization was found to be an effective numerical technique for solving the model equations. An argonlike (electropositive) discharge was compared to a pure chlorine (electronegative) discharge. The electronegative discharge was found to have much thinner sheaths, much greater potential drop and electric field strength in the bulk plasma, and severe modulation by the applied rf (10 MHz frequency) of the electron temperature, ionization, and excitation rate, even in the bulk. The effect of varying excitation frequency was also examined. The results showed that continuum models can capture the essential features of both kinds of discharges. Integration of these models with neutral species transport and reaction can result in powerful tools for the modeling and design of plasma reactors.

I. INTRODUCTION

Plasma etching and deposition of thin solid films using low pressure radio frequency (rf) glow discharges is currently in widespread use in the microelectronics industry. In this method, an otherwise inert feedstock gas is excited in an electric discharge to produce reactive atoms and radicals by electron-impact dissociation of the parent gas.¹ The radical density and its spatial distribution are strongly affected by the energy and density distributions of the plasma electrons. The radicals interact with the substrate to form volatile products, thereby etching the substrate, or adsorb and react to deposit a thin film. The surface reactions are modified by energetic particle (especially positive ion) bombardment. It is due to this ion bombardment that plasma etching is capable of anisotropic (or directional) etching, resulting in faithful reproduction of resist patterns into the underlying film. In the case of plasma deposition, ion bombardment can have a profound effect on the deposited film microstructure and properties. The ion bombardment flux and energy are strongly influenced by the potential distribution and ion transport and reaction in the plasma sheath. It follows that the potential distribution and the charged particle transport and reaction is of paramount importance in determining the outcome of the plasma process.

Reactive gas plasmas are notoriously complex systems owing to the nonequilibrium nature of the discharge, and the intricate coupling between potential distribution, particle (charged and neutral) transport, and multiple chemical reactions for which kinetic information is scarce. In order to make the analysis more tractable one may divide the overall problem into two separate problems; namely, the problem of potential distribution and charged particle transport on one hand, and that of neutral species transport and reaction on the other. By this separation one can focus either on the physical aspects or chemical aspects of the discharge. Neu-

tral species transport and reaction is a problem of chemically reactive gas flow, and as such is rather well developed, especially in the context of combustion. For this problem, the role of the plasma is simply as a source of reactive radicals. However, the problem of potential distribution and charged particle transport is still in its infancy. It is this problem that is the subject of this work. Of course, ultimately, one has to combine the two problems to arrive at a self-consistent model of the gas discharge.

Continuum (fluid) models of charged particle transport and potential distribution appear to be useful in the effort to understand the physical structure of the discharge. In these models, equations of continuity are written for the electron and ion density, momentum, and energy. The continuity equations are coupled to the Poisson equation relating the potential field to the charge density. If a magnetic field is also present, the Maxwell equations for the electromagnetic field must be written. Reactions are usually limited to ionization and excitation. In the case of electronegative discharges, attachment and ion-ion recombination are also included. Depending on the gas pressure, continuum models may not yield accurate results, especially in the plasma sheath, where the electric field changes rapidly in both space and time. In such cases, particle simulations² based on the Monte Carlo or other methods may be a useful alternative.

The continuum models of interest consist of a set of time-dependent partial differential equations which are stiff in both space and time. In order to simplify the problem several assumptions and approximations are usually introduced. The most commonly used assumptions are the one-dimensional spatial approximation, the replacement of the particle momentum equations by expressions for the total particle flux (diffusion plus drift), and the omission of the ion energy (temperature) equation. In addition, the electron energy distribution function is not found. Graves and Jensen³ and Graves⁴ used the above assumptions to calculate the electron density and temperature distribution, potential field and current density, and excitation waveforms in an argonlike rf discharge. Richards *et al.*⁵ used a similar approach except that they introduced an effective electric field

^{a)} Present address: Motorola Inc., MD:K-10, 3501 Ed Bluestein Blvd., Austin, TX 78721.

^{b)} Author to whom correspondence should be addressed.

to which the massive ions respond. Barnes *et al.*⁶ introduced an equation for the electron momentum. Boeuf⁷ studied both a helium discharge and a model electronegative discharge. He used the local equilibrium approximation, omitting the electron energy equation. Boeuf studied the effect of applied potential and frequency. Gogolides *et al.*⁸ compared temporally resolved optical emission profiles to calculations in argon and SF₆ discharges.

Despite the simplifying assumptions, the model equations are difficult to solve because the equations are still stiff in both space and time. The numerical complexities limit the range of applicability of the models, and the excessive CPU time needed to solve the equations prohibits effective utilization of the models. These difficulties become more apparent as additional reactions are included with a great disparity in time scales. Until now reported results are usually limited to a single set of operating conditions. An exception is the work of Boeuf⁷ who examined the effect of applied voltage and frequency.

In the present work, an effective numerical algorithm was employed to solve the continuity equations describing charged particle transport and potential distribution in low pressure rf glow discharges. An argonlike discharge was examined as an example of an electropositive discharge. The effect of applied voltage and frequency was studied. The effect of pressure and electrode spacing was reported elsewhere.⁹ A chlorine discharge was also investigated as an example of an electronegative discharge. Two different excitation frequencies were examined. The strikingly different characteristics of the two discharges were compared. The model formulation is described in Sec. II, and the method of solution is given in Sec. III. Section IV contains the results and discussion, and Sec. V contains the summary and conclusions.

II. MODEL FORMULATION

The set of model equations for both electropositive and electronegative discharges is presented first. The discussion then focuses on each kind of discharge separately. The basic assumptions of the model are as follows: (1) the discharge is formed between two large-area parallel conductive electrodes so that a one-dimensional spatial approximation is permissible, (2) the particle motion is collision-dominated, and a continuum approximation may be used, (3) the electron energy distribution function is Maxwellian, (4) the particle diffusivity and mobility are constant for a given gas number density, (5) for the electropositive discharge, the main reactions are ionization and excitation of the neutral gas, and the reaction rate constants have an Arrhenius dependence on electron temperature; for the electronegative discharge, electron attachment and ion-ion recombination are also included, and (6) the gas temperature is constant at 273 K. Under these assumptions the model equations are written as

$$\frac{\partial n_e}{\partial t} + \nabla \cdot \mathbf{J}_e = R_i - R_a, \quad (1)$$

$$\frac{\partial n_{\pm}}{\partial t} + \nabla \cdot \mathbf{J}_{\pm} = R_{\pm} - R_{\pm}, \quad (2)$$

$$\frac{\partial n_{-}}{\partial t} + \nabla \cdot \mathbf{J}_{-} = R_a - R_{\nu}, \quad (3)$$

$$\mathbf{J}_e = -D_e \nabla n_e + n_e \mu_e \nabla V, \quad (4)$$

$$\mathbf{J}_{+} = -D_{+} \nabla n_{+} - n_{+} \mu_{+} \nabla V, \quad (5)$$

$$\mathbf{J}_{-} = -D_{-} \nabla n_{-} + n_{-} \mu_{-} \nabla V, \quad (6)$$

$$\frac{\partial}{\partial t} \left(\frac{3}{2} n_e k T_e \right) + \nabla \cdot \mathbf{q}_e - e \mathbf{J}_e \cdot \nabla V + \sum_j H_j R_j = 0, \quad (7)$$

$$\mathbf{q}_e = -K_e \nabla T_e + \frac{3}{2} k T_e \mathbf{J}_e, \quad (8)$$

$$\nabla^2 V = -\frac{e}{\epsilon_0} (n_{+} - n_e - n_{-}). \quad (9)$$

Equations (1), (2), and (3) are the electron, positive ion, and negative ion continuity equations, respectively. Equations (4), (5), and (6) are in essence the momentum balance for the electrons, positive ions, and negative ions, respectively. Equation (7) is the electron energy balance, with the total electron energy flux given by Eq. (8). Equation (9) is the Poisson equation for the potential distribution in the gap. In the above equations, n_e , n_{+} , and n_{-} are the electron, positive ion, and negative ion density, respectively, \mathbf{J}_e , \mathbf{J}_{+} , and \mathbf{J}_{-} are the electron, positive ion, and negative ion flux, respectively, T_e is the electron temperature, and \mathbf{q}_e is the electron energy flux. R_i , R_a , and R_{ν} are the ionization, attachment and ion-ion recombination rates, respectively. Moreover, V is the electrostatic potential, and D_j ($j = e, +, -$), and μ_j ($j = e, +, -$) are the particle diffusivity and mobility, respectively. In Eq. (7), the summation is over the reactions involving inelastic electron collisions, and H_i is the electron energy loss per collision. Finally, ϵ_0 is the permittivity of the free space.

Boundary conditions were as follows: At $x = 0$ (surface of left electrode)

$$J_e = k_r n_e - \gamma J_{+}, \quad (10)$$

$$J_{+} = -n_{+} \mu_{+} \nabla V, \quad (11)$$

$$n_{-} = 0, \quad (12)$$

$$T = T_{ec}, \quad (13)$$

$$V = -V_{rf} \sin(2\pi ft), \quad (14)$$

and at $x = L$ (surface of right electrode)

$$J_e = k_r n_e - \gamma J_{+}, \quad (15)$$

$$J_{+} = -n_{+} \mu_{+} \nabla V, \quad (16)$$

$$n_{-} = 0, \quad (17)$$

$$T_e = T_{ea}, \quad (18)$$

$$V = 0.0. \quad (19)$$

Here k_r is the electron surface recombination coefficient calculated assuming an electron sticking coefficient of unity, γ is the secondary electron emission coefficient, V_{rf} is the peak rf voltage, L is the interelectrode spacing, and f is the excitation frequency. The boundary condition on the electron temperature is difficult to specify.⁴ A simplified constant temperature condition was used in the present study.

A. Electropositive discharge

An argonlike discharge was studied as an example of an electropositive discharge. In this case the negative ion den-

sity was set equal to zero everywhere. Therefore, Eqs. (3) and (6) were omitted. The attachment rate in Eq. (1) and the recombination rate in Eq. (2) were set equal to zero. In Eq. (7), the summation included ionization and excitation. The reactions can be represented schematically as



The corresponding reaction rates were expressed as a function of the electron temperature in an Arrhenius form as shown in Eqs. (22) and (23) below:

$$R_i = k_{i0} n_e N \exp(-E_i/kT_e), \quad (22)$$

$$R_{\text{ex}} = k_{\text{ex}0} n_e N \exp(-E_{\text{ex}}/kT_e), \quad (23)$$

where k_{i0} and $k_{\text{ex}0}$ are the pre-exponential coefficients, and E_i and E_{ex} are the corresponding activation energies, respectively. N is the neutral gas density ($=p/kT$, where p is the gas pressure, k is the Boltzmann constant, and T is the gas temperature = 273 K). The values of the parameters used for the electropositive discharge are shown in the third column of Table I.⁴ The use of the term "argonlike" reflects the fact that argon metastables were not considered. For example, metastable atoms can make a significant contribution to the ionization rate. However, it was felt that the essential features of the discharge could be captured, despite the fact that metastables were omitted.

B. Electronegative discharge

A chlorine discharge was studied as an example of an electronegative discharge. In this case rapid electron attachment creates a large concentration of negative ions.¹⁰ The reactions considered are electron (dissociative) attachment [Eq. (24)], ionization [Eq. (25)], excitation [Eq. (26)] and ion-ion recombination [Eq. (27)]:



Excitation to the $C_1\Pi$ state (which is dissociative) was taken as a representative excitation channel for the Cl_2 discharge. Cl_2^+ is thought to be the main positive ion,^{10,11} and Cl^- the main negative ion¹⁰ in the discharge. An important assumption was that the Cl density in the discharge was low (small degree of Cl_2 dissociation) and did not affect the discharge properties. This assumption is expected to be better for lower power input. The rate expressions corresponding to Eqs. (24)–(27) were written as

$$R_a = k_a N n_e, \quad (28)$$

$$R_i = k_i N n_e, \quad (29)$$

$$R_{\text{ex}} = k_{\text{ex}} N n_e, \quad (30)$$

$$R_r = k_r n_+ n_-. \quad (31)$$

The rate constants for ionization and excitation were taken as

$$k_i = \begin{cases} 8 \times 10^{-15} & \text{if } T_e < 1.35 \text{ eV} \\ 3.095 \times 10^{-8} \exp\left(\frac{-3.3403}{T_e} - \frac{42.105}{T_e^2}\right) \\ + \frac{81.313}{T_e^3} - \frac{75.338}{T_e^4} & \text{if } T_e > 1.35 \text{ eV}, \end{cases} \quad (32)$$

$$k_{\text{ex}} = 3.344 \times 10^{-8} \exp\left(\frac{-0.75773}{T_e} - \frac{8.1738}{T_e^2} + \frac{1.0712}{T_e^3}\right). \quad (33)$$

TABLE I. Parameter values.

Name	Symbol	Ar-like	Cl_2
Electron diffusivity	ND_e (cm s) ⁻¹	1.7×10^{22}	3.21×10^{22}
Positive ion diffusivity	ND_+ (cm s) ⁻¹	8.0×10^{17}	3.95×10^{17}
Negative ion diffusivity	ND_- (cm s) ⁻¹	...	4.89×10^{17}
Electron mobility	$N\mu_e$ (V cm s) ⁻¹	8.5×10^{21}	6.42×10^{21}
Positive ion mobility	$N\mu_+$ (V cm s) ⁻¹	3.6×10^{19}	1.52×10^{19}
Negative ion mobility	$N\mu_-$ (V cm s) ⁻¹	...	1.88×10^{19}
Ionization pre-exponential factor	k_{i0} (cm ³ /s)	1×10^{-7}	Eq. (32)
Activation energy	E_i (eV)	17.7	Eq. (32)
Energy loss	H_i (eV)	17.7	11.5
Excitation pre-exponential factor	$k_{\text{ex}0}$ (cm ³ /s)	5×10^{-9}	Eq. (33)
Activation energy	E_{ex} (eV)	11.6	Eq. (33)
Energy loss	H_{ex} (eV)	11.6	3.12
Secondary electron coefficient	γ	0.05	0.05
Wall electron temperature	T_{ec} (eV)	0.5	1.0
Volume recombination coefficient	k_r (cm ³ /s)	...	5×10^{-8}
Attachment coefficient	k_a (cm ³ /s)	...	1.8×10^{-10}

The above expressions are fits to values of the rate constants calculated by solving the Boltzmann transport equation.^{10,12} The equation was solved for different values of E/N , and the corresponding electron energy distribution function $f(\epsilon)$ was found. The rate constants were then calculated from the known cross section $\sigma_j(\epsilon)$ for process j using the expression

$$k_j = \int_0^\infty f(\epsilon) \sigma_j(\epsilon) u(\epsilon) d\epsilon, \quad (34)$$

where $u(\epsilon)$ is the electron velocity, and ϵ is the electron energy. The mean electron energy was also calculated as a function of E/N . In order to derive the fits shown in Eqs. (32) and (33), the corresponding electron temperature was taken as 2/3 of the calculated mean electron energy. The values of the rest of the parameters used for the chlorine discharge are shown in the fourth column of Table I.

III. METHOD OF SOLUTION

The problem consists of determining the electron, positive ion, and negative ion density, electron temperature, and potential as a function of space and time in the gap for a given

set of system parameters. Current density, power dissipation, excitation and ionization rates, and other derived quantities may then be obtained. The problem requires solution of the coupled system of parabolic [Eqs. (1), (2), (3), and (7)] and elliptic [Eq. (9)] partial differential equations (PDE) subject to the appropriate boundary conditions [Eqs. (10)–(19)] and initial conditions (to be given later). This system of PDEs was solved by the method of lines.^{13–15} In this method, the spatial derivatives are discretized by using finite difference or finite element approximations. Thus, the nodal values of each dependent variable become unknown functions of time. In this work, the equations were discretized in the spatial direction using orthogonal collocation on finite elements,¹⁴ with *B*-spline (cubic polynomial) basis functions.^{16,17} After discretization, Eqs. (1), (2), (3), and (7) resulted in a system of ordinary differential equations (ODEs), whereas Eq. (9) resulted in a system of algebraic equations.

A system of coupled parabolic and elliptic PDEs in one spatial dimension *x* may be represented by

$$\frac{\partial \mathbf{C}}{\partial t} = \mathbf{f}(t, \mathbf{x}, \mathbf{C}, \mathbf{C}_x, \mathbf{C}_{xx}, \mathbf{P}), \quad (35)$$

$$\mathbf{O} = \mathbf{g}(t, \mathbf{x}, \mathbf{C}, \mathbf{C}_x, \mathbf{C}_{xx}, \mathbf{P}), \quad (36)$$

where

$$\mathbf{x} \in [x_L, x_R], \quad t \in [t_0, t_f],$$

and

$$\mathbf{C} = \{C_i\}_{i=1}^{N_{\text{PDE}}}, \quad \mathbf{C}_x = \{C_{xi}\}_{i=1}^{N_{\text{PDE}}},$$

and

$$\mathbf{C}_{xx} = \{C_{xxi}\}_{i=1}^{N_{\text{PDE}}}.$$

C_i , C_{xi} , and C_{xxi} are the *i*th dependent variable (e.g., density of species *i*), its first derivative, and its second derivative respectively, \mathbf{P} is a vector of parameters (e.g., D_j , k_j), \mathbf{f} and \mathbf{g} are vector-valued functions for the parabolic and elliptic system, respectively, x_L and x_R are the left-most and right-most point in the spatial domain, respectively; t_0 and t_f are the initial and final time, respectively, and N_{PDE} is the number of PDEs. The boundary conditions at each boundary point may be expressed as

$$\mathbf{B}(t, \mathbf{C}, \mathbf{C}_x) = \mathbf{0}, \quad t \in [t_0, t_f], \quad (37)$$

where \mathbf{B} is a vector of dimension N_{PDE} , and \mathbf{C} and \mathbf{C}_x are evaluated at the corresponding boundary point. The initial condition may be written as

$$\mathbf{C}(t_0, \mathbf{x}) = \mathbf{C}_0(\mathbf{x}), \quad \mathbf{x} \in (x_L, x_R), \quad (38)$$

where \mathbf{C}_0 is again a vector of dimension N_{PDE} , with $\mathbf{C}_0(\mathbf{x})$ known. It is assumed that all functions are continuous in time and at least piecewise continuous in space.

In the present work, the spatial domain was divided into N_e elements, and each unknown dependent variable was expanded in terms of a set of piecewise *B*-spline basis functions^{16,17}

$$C_i(\mathbf{x}, t) = \sum_{j=1}^{N_b} a_{ij}(t) B_j^{kn}(\mathbf{x}), \quad i = 1, N_{\text{PDE}}, \quad (39)$$

where N_b is the number of *B*-spline collocation points, B_j^{kn} is

a polynomial of degree *k* (and $n - 1$ continuity) on each element $[x_l, x_{l+1}]$, $l = 1, N_e$, with $x_1 = x_L$ and $x_{N_e+1} = x_R$; x_l and x_{l+1} define the endpoints of element *l*, and a_{ij} is the time-dependent unknown coefficient of variable C_i at point *j*. This is the so-called collocation on finite elements method.¹⁴ The collocation points were chosen such that

$$x_L = x_1 = \xi_1 < \xi_2 < \dots < \xi_m < \dots < \xi_{N_b} = x_{N_e+1} = x_R \quad (40)$$

and

$$B_j^{kn}(\xi_m) = \begin{cases} 0 & \text{for } j \neq m \\ \neq 0 & \text{for } j = m, \end{cases} \quad m = 1, 2, \dots, N_b. \quad (41)$$

By substituting Eq. (39) into Eqs. (35) and (36), and implementing the boundary condition Eq. (37), leads to a system of $N_{\text{PDE}} \times N_b$ time-dependent differential/algebraic equations for the components of the unknown vector *a*.

$$\mathbf{A} \frac{d\mathbf{a}}{dt} = \mathbf{F}(t, \mathbf{a}, \mathbf{P}), \quad (42)$$

$$\mathbf{0} = \mathbf{G}(t, \mathbf{a}, \mathbf{P}), \quad (43)$$

where \mathbf{A} is a known matrix and \mathbf{F} and \mathbf{G} are known functions of *t* and *a*. Equations (42) and (43) can be combined as

$$\mathbf{A}^* \frac{d\mathbf{a}}{dt} = \mathbf{F}^*(t, \mathbf{a}, \mathbf{P}). \quad (44)$$

The matrix \mathbf{A}^* has a maximum bandwidth of $[2(k - 1)N_{\text{PDE}} - 1]$.

The initial condition is found by substituting Eq. (39) into Eq. (38) to yield a relation of the form:

$$\mathbf{a} = \mathbf{a}_0 \text{ at } t = t_0. \quad (45)$$

In this work, the resulting differential/algebraic equation system (DAES) was solved by using LSODI.^{18–20} The routine uses a backward difference formula with automatically variable order and variable time-step size, controlled by estimating the time discretization error. Fifty finite elements were used, with smaller element size near the electrodes, where steep gradients are expected. For the electropositive discharge this resulted in a system of 408 equations (306 ODEs resulting from the electron continuity, positive ion continuity, and electron energy balance, and 102 algebraic equations resulting from Poisson's equation). For the electronegative discharge the result was 510 equations (including 102 ODEs for the negative ion density). The harmonic steady state was detected by defining a convergence criterion based on the electron temperature

$$\epsilon_{\text{pss}} = \left\{ \sum_{j=1}^{N_b} \left[\left(\frac{T_{e,j}}{T_{e,\text{av}}} \right)_{(j+1)\tau_{\text{rf}}} - \left(\frac{T_{e,j}}{T_{e,\text{av}}} \right)_{j\tau_{\text{rf}}} \right]^2 / N_b^2 \right\}^{1/2}, \quad (46)$$

where $T_{e,j}$ and $T_{e,\text{av}}$ are the electron temperature at collocation point *j* and the spatially average electron temperature respectively, τ_{rf} is the rf period, and ϵ_{pss} is a user-specified error tolerance. The electron temperature was chosen to test convergence (instead of, for example, the particle density) since the results are very sensitive to T_e (e.g., exponential dependence of reaction rate on T_e), and since the T_e profiles show sharp peaks near the plasma-sheath interface, making for a stricter convergence test.

The following initial conditions were used:

$$n_e = n_+ = 10^7 + 10^9(1 - x/L)^2(x/L)^2, \text{ cm}^{-3}, \quad (47)$$

$$T_e = 1.0 \text{ eV}, \quad V = 0 \text{ V}, \quad (48)$$

and the initial time-step size was set at 10^{-14} s. Equation (47) was used for the electropositive discharge. For the electronegative discharge, the initial condition was such that $n_e = n_- = 2n_+$.

Calculations were performed in double precision on an NEC SX-2 supercomputer. For the electropositive discharge, for a pressure of 1 Torr and a spacing of 3 cm, the execution time was 20 CPU mins, for a value $\epsilon_{\text{pss}} = 10^{-5}$. The execution time can be further reduced by considering only half of the interelectrode gap.⁴ After obtaining a converged solution, a continuation method can be used to study the effect of parameter changes, reducing drastically the CPU time requirements.

Results reported for the electronegative Cl_2 discharge are those obtained after 1000 cycles, which took nearly $1\frac{1}{2}$ h of CPU time. The rate of convergence was substantially lower compared to the electropositive discharge due to the long time scale of negative ion reactions. Complete convergence was not achieved. The positive and negative ion densities increased slowly, whereas the electron density changed even more slowly. However, it is believed that the results will not change significantly at full convergence. Similar convergence difficulties were experienced by Gogolides *et al.*⁸ when modeling an SF_6 discharge which is also strongly electronegative.

IV. RESULTS AND DISCUSSION

A. Electropositive discharge

Parameter values used for the electropositive argonlike discharge are shown in the third column of Tables I and II. The basic operating conditions were: pressure 1 Torr, excitation frequency 10 MHz, and peak rf voltage 25 V (50 V peak-to-peak). The effects of frequency (1 MHz and 100 MHz), and of applied peak voltage (50 V) were also examined. Operating conditions were varied one at a time, keeping the other operating conditions at their basic value. Much of the results reported for the electropositive discharge have been observed before,³⁻⁵ but are included here for the sake of completeness, and for the purpose of comparing the electropositive to the electronegative discharge.

Figure 1 shows the electron density distribution in the interelectrode space at four different times in the rf cycle. Time T was normalized with respect to the rf period. Time

TABLE II. Operating conditions.

Name	Symbol	Ar-like	Cl_2
Gas pressure	P (Torr)	1.0	0.5
Interelectrode spacing	L (cm)	3.0	3.0
rf peak voltage	V_{rf} (V)	25, 50	150
rf frequency	f (MHz)	1, 10, 100	10, 100
Gas temperature	T (K)	273	273

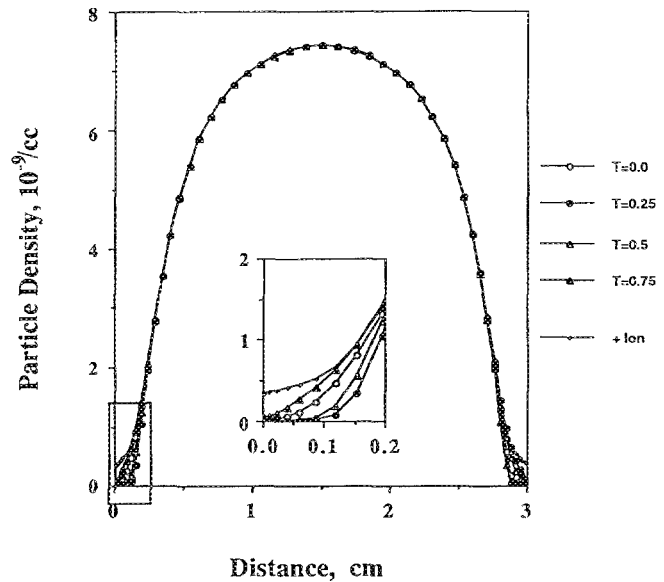


FIG. 1. Spatial and temporal variation of electron and positive ion density for the electropositive discharge. Conditions were at their basic value. Inset shows an expanded view of the sheath region.

$T = 0$ corresponds to the negative zero crossing of the rf voltage applied to the left electrode, i.e., at time $T = 0.25$ the left electrode is at its peak negative potential. One observes that the electron density is modulated substantially near the electrodes, with the electrons repelled by the momentary cathode ($T = 0.25$, left electrode) and attracted by the momentary anode ($T = 0.75$, left electrode). Electron density modulation in the bulk of the discharge is much weaker and cannot be resolved on the scale used for Fig. 1. The electron density distribution is seen to have a cosinelike shape. However, electron density profiles which are flatter in the bulk can be obtained by increasing the gas pressure or the electrode spacing.⁹ The ion density is not modulated by the rf since the ions are too massive to respond to the rapidly changing field. The time-average electron and positive ion profiles were symmetric since there was no dc bias applied to the electrode. The time-average sheath was found to be a few mm thick under the present conditions.

The potential distribution in the gap is shown in Fig. 2. The left electrode ($x = 0$ cm) potential oscillates according to the applied sinusoidal waveform, while the right electrode ($x = 3$ cm) is always at ground (zero) potential. At any time during the rf cycle, the potential of the bulk (plasma potential) is seen to be more positive than the potential of either electrode. The potential drop in the bulk is comparatively small, since the mobile electrons provide for a high conductivity in the bulk. However, a sharp potential drop is seen in the plasma sheath, especially when the electrode is the momentary cathode ($T = 0.25$ at $x = 0$ cm, and $T = 0.75$ at $x = 3$ cm). The corresponding electric field distribution is shown in Fig. 3. The electric field is rather weak in the bulk plasma, since the bulk plasma is a nearly equipotential volume. However, relatively strong electric fields develop in the sheath, and the sheath electric field is severely modulated by the rf. It is the strong sheath electric field which is of paramount importance in plasma etching. For example, ions ac-

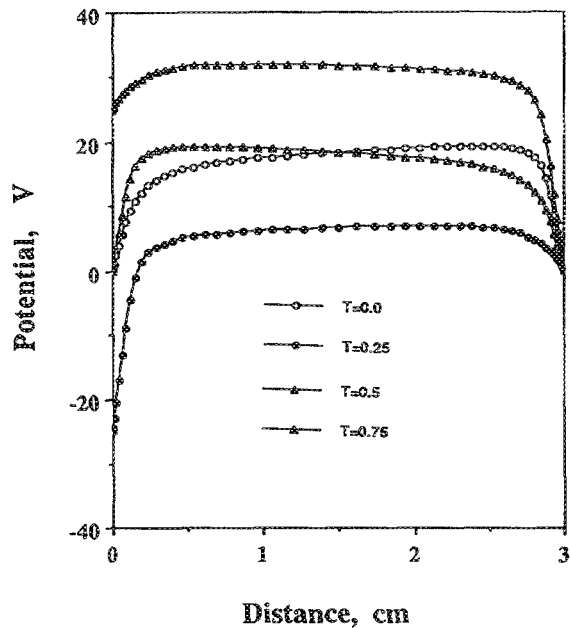


FIG. 2. Spatial and temporal variation of the potential for the electropositive discharge. Conditions were at their basic value.

celerate under the influence of this field and bombard the wafer surface with high kinetic energy, inducing anisotropic etching. The ion bombardment energy may be lower than the average sheath voltage since ions can experience collisions with neutrals as the ions cross the sheath. Figure 4 shows the applied voltage and the resulting current waveform. The current lags the voltage by about 80° . Hence the discharge is primarily capacitive with a small resistive component. The capacitance arises because of the wide plasma sheaths, where most of the applied voltage is dropped.

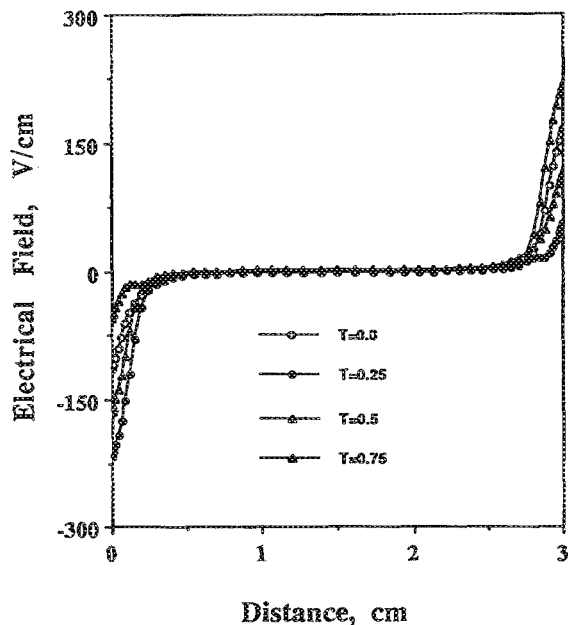


FIG. 3. Spatial and temporal variation of the electric field for the electropositive discharge. Conditions were at their basic value.

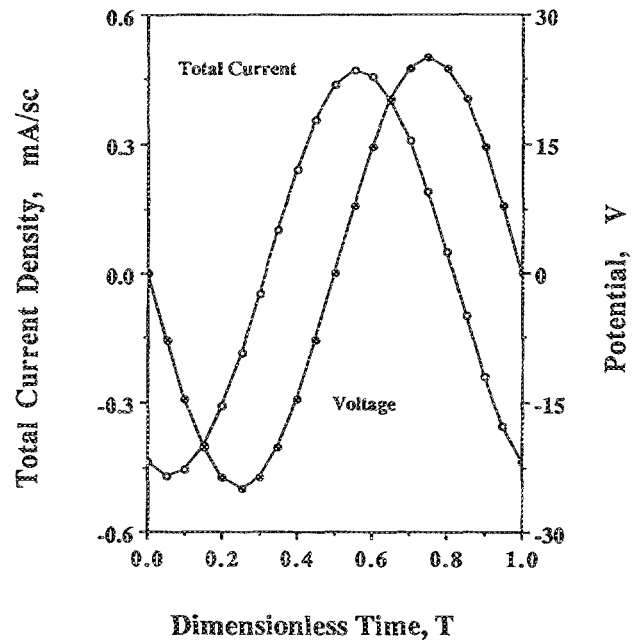


FIG. 4. Total current and voltage waveforms for the electropositive discharge. Conditions were at their basic value.

The electron temperature distribution is shown in Fig. 5, at different times during the rf cycle. One observes much higher temperatures and steep temperature gradients near the plasma-sheath interface. Electrons which diffuse towards the electrode during the anodic part of the cycle ($T = 0.5-1.0$ at left electrode, see also Fig. 1) are pushed back into the plasma as the potential reverses during the cathodic part of the cycle. One can think of the electrons "riding the wave" as the sheath boundary moves away from the electrode during the cathodic part of the cycle. The electric field in the bulk plasma is much weaker than that in the

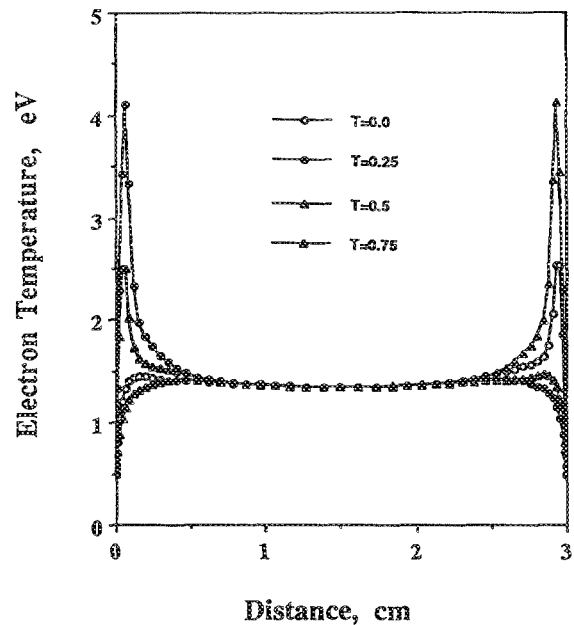


FIG. 5. Spatial and temporal variation of the electron temperature for the electropositive discharge. Conditions were at their basic value.

sheath. Hence the bulk electron temperature is lower. In addition, despite the severe modulation in the sheath, the bulk electron temperature is nearly time independent. One should note at this point that "beam electrons," resulting from secondary electron emission by ion impact of the electrodes, are not expected to play a role in this relatively high pressure, high frequency discharge. The effect of secondary emission coefficient was not examined (a constant value of 0.05 was used). However, secondary electrons are not expected to penetrate the plasma bulk because the electron mean free path is small under the present conditions (of the order of 100μ).

The ionization [Eq. (20)] and excitation [Eq. (21)] rate profiles are shown in Figs. 6(a) and 6(b), respectively. Owing to symmetry, only the left half of the interelectrode space is shown. The profiles in the right half may be found by flipping the plot around the axis $x = 1.5$ cm, and adding 0.5 to T . Very near the electrode, the electron temperature may be higher than that in the bulk (Fig. 5), hence the rate coefficients are also higher. However, the electron density is very low resulting in low ionization and excitation rate [Eq. (22) and (23)]. Further away from the electrode, the electron temperature is still higher than that in the bulk, and the electron density is now appreciable. This results in high ionization and excitation rates especially around the plasma-sheath interface. This is in accord with experimental observations of the discharge showing areas of brighter plasma emission a few mm from the electrodes. A double peak in the ionization rate is observed especially when the electrode potential has its maximum negative value ($T = 0.25$). The first peak (nearer the electrode) is associated with the peak in electron temperature (Fig. 5, $T = 0.25$). The electron density nearer the electrode is lower, and this is the reason the first peak is lower than the second peak. The second peak forms further away from the electrode where the electron density is higher, and yet the electron temperature has not

decayed to its lowest (bulk) value. Moreover, closer examination of Fig. 6 reveals that both the ionization and the excitation rate are slightly modulated in the bulk plasma.

Figure 7 shows the effect of applied voltage. Again only the left half of the interelectrode space is shown. Other operating conditions were at their basic value (1 Torr, 10 MHz). Increasing the discharge voltage amounts to higher power input to the discharge. This results in higher electron (and ion) density. Figure 7(a) shows the time-average potential in the gap. As expected the plasma potential (say that at $x = 1.5$ cm) increases as the applied voltage (power) increases. In symmetric discharges (such as the one examined here), the time-average plasma potential is often taken to be one-half the applied peak rf voltage.²¹ As seen in Fig. 7(a), this approximation becomes better the higher the applied voltage. This is because the plasma potential is always a few volts above ground (see Fig. 2), and this adds to the time-average plasma potential. The corresponding time-average electron temperature is shown in Fig. 7(b). The electron temperature near the plasma-sheath interface is a strong function of the applied voltage, since this temperature is determined by the sheath electric field. However, the bulk electron temperature is a weak function of the applied voltage. This implies that changing power primarily affects the electron density and has little effect on bulk electron temperature. This may be expected for the relatively high pressure discharge examined. Under such conditions, secondary electrons can not penetrate the bulk plasma. However, the situation may be different in relatively low pressure, low frequency discharges where beam electrons can play a role. Figure 7(c) shows the time-average electric field distribution in the gap. The sheath electric field increases sharply with increasing applied voltage (power). Hence one expects more energetic ion bombardment as the power to the discharge increases. One further observes that the bulk electric field is not affected significantly by changing the applied voltage. This is because most of the applied voltage is dropped across the sheath.

The effect of applied frequency is shown in Fig. 8. Other operating conditions were kept at their basic value (1 Torr, 25 V peak). Figure 8(a) shows the time-average electric field for frequencies of 1, 10, and 100 MHz. As frequency increases, the plasma sheath becomes thinner, and the sheath electric field increases (since the applied voltage was kept constant, and most of the voltage is dropped across the sheath). The reduction in sheath thickness with increasing frequency is a well-known experimental fact. Figure 8(b) shows the time-average electron temperature. The bulk electron temperature increases with increasing frequency. This implies that the higher the frequency the more efficient the discharge in terms of ionization (and dissociation in the case of molecular gas discharges) in the bulk. The peak electron temperature near the electrode appears to pass through a maximum as the frequency increases. It was found that, as frequency increased at constant applied voltage, the electron density increased, with a concomitant increase of the power deposited in the discharge. In addition, the electron density profile was found to become flatter in the bulk plasma as frequency increased.

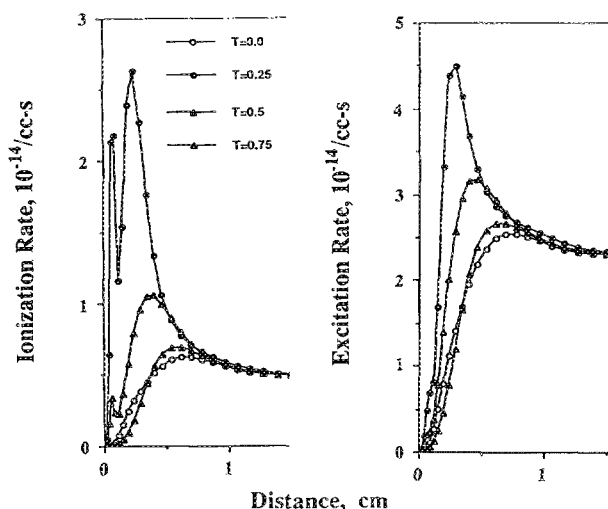


FIG. 6. Spatial and temporal variation of the ionization rate and excitation rate for the electropositive discharge. Conditions were at their basic value.

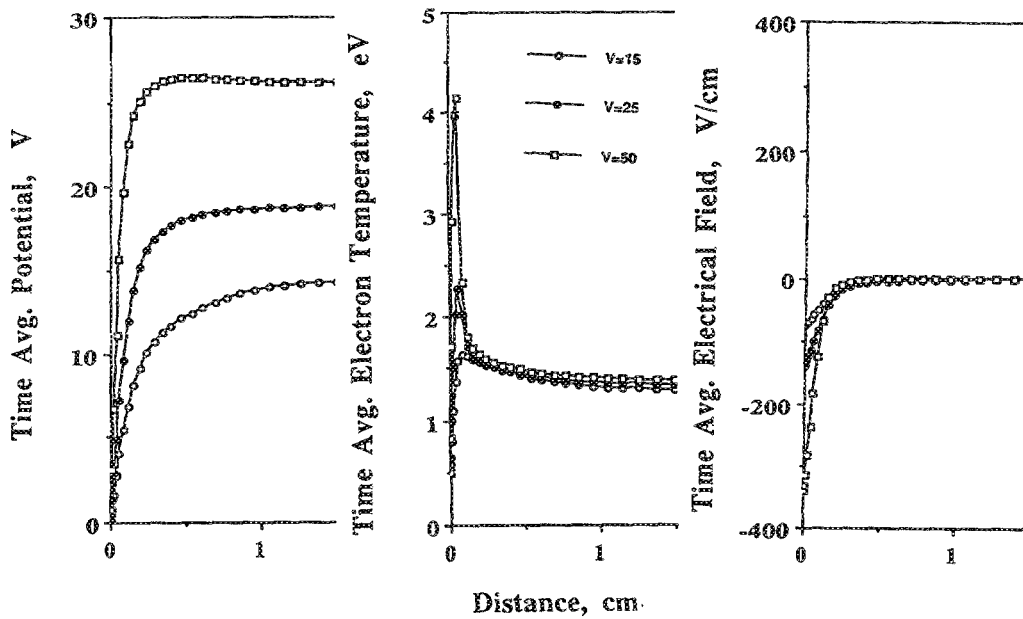


FIG. 7. Spatial and temporal variation of potential time-average electron temperature and time-average electric field as a function of position in the gap for the electropositive discharge. Conditions were at their basic value except for the applied rf voltage.

The conditions used for the electropositive discharge were closest to those of Ref. 4. There exists good qualitative agreement between the results of the present study and those of Ref. 4. Direct quantitative comparison is not possible because the pressure, electrode spacing, and applied voltage are different in the two studies.

B. Electronegative discharge

Parameter values used for the electronegative (chlorine) discharge are shown in the fourth column of Tables I and II. The basic operating conditions were: pressure 0.5 Torr, excitation frequency 10 MHz, spacing 3 cm, and peak rf voltage 150 V (300 V peak-to-peak). A discharge frequen-

cy of 100 MHz was also examined, keeping the other operating conditions at their basic value. A similar model for an electronegative discharge was recently presented by Oh *et al.*²² The authors considered an argonlike discharge containing negative ions.

Figure 9 shows the space and time dependence of the electron and ion concentrations. The electron density profiles are modulated by the rf, mainly in the sheath. Some modulation is observed in the bulk as well, in contrast to the electropositive discharge (Fig. 1). However, the massive

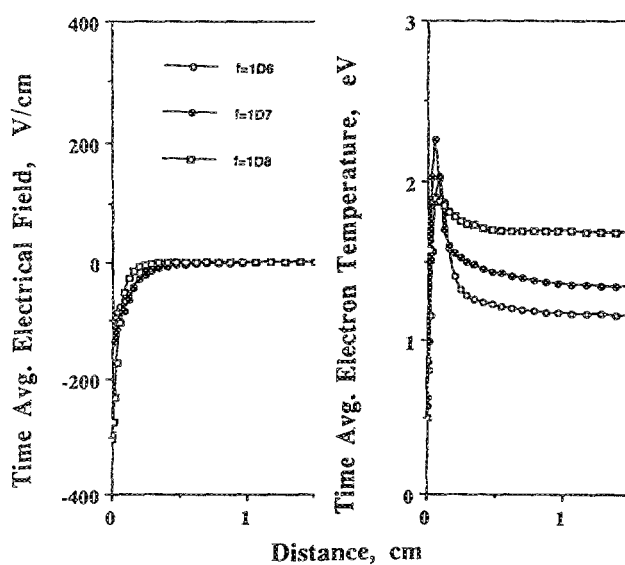


FIG. 8. Time-average electric field and time-average electron temperature as a function of position in the gap for the electropositive discharge. Conditions were at their basic value except for the rf frequency.

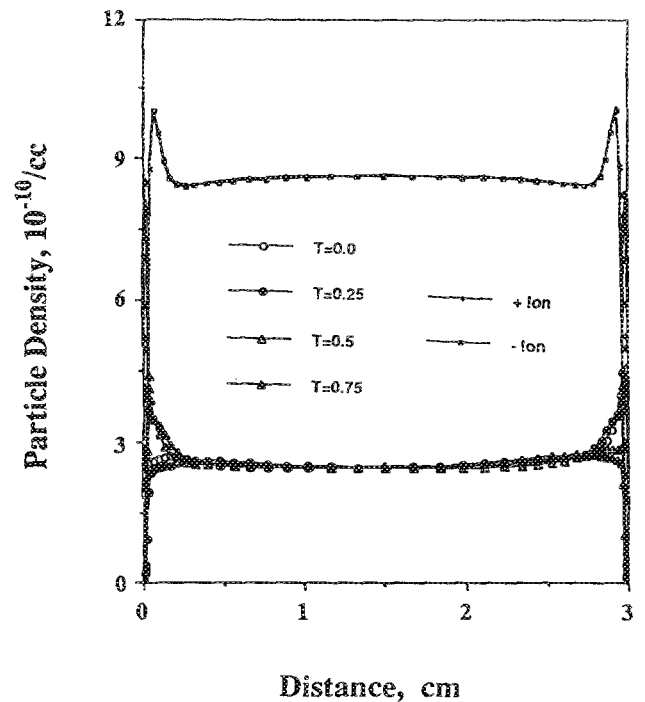


FIG. 9. Spatial and temporal variation of electron, positive ion, and negative ion density for the electronegative discharge. Condition were at their basic value. The electron density has been multiplied by 100.

ions do not respond to the rapid variations of the field. Hence, the ion density profiles are nearly time independent. One observes a large concentration of negative ions compared to electrons. This is a result of the electron attachment reaction [Eq. (24)] which is very rapid in chlorine. Since the negative ion density is more than two orders of magnitude higher than the electron density, the condition of quasi-neutrality in the plasma bulk necessitates equal positive and negative ion densities there. However, the negative ions are excluded from the plasma sheath, as long as the plasma potential remains positive with respect to the electrode potential. The charged particle concentration profiles are completely different in the electronegative discharge (compare to Fig. 1). The electrons seem to be trapped near the plasma-sheath interface. A peak in the ion density profiles appears as well. The existence of a peak in the negative ion density near the plasma-sheath interface was postulated by Selwyn *et al.*²³ to explain their laser-induced fluorescence results in a chlorine discharge. Furthermore, the electron density in the bulk plasma is nearly flat. This is again a result of the large concentration of negative ions. Under such condition, the electron ambipolar diffusivity is almost equal to the free electron diffusivity.²⁴ The high electron diffusivity promotes more uniform electron density profiles.

The potential distribution in the gap is shown in Fig. 10, at different times during the cycle. There exist striking differences between the electronegative and the electropositive discharge (compare to Fig. 2). First, the bulk plasma is no longer a nearly equipotential volume. Instead, a large potential drop is seen across the bulk. Since the electron density is low, the plasma resistance is correspondingly high (the ion density is much higher, but the ion mobility is low). This accounts for the large potential drop. Second, the plasma

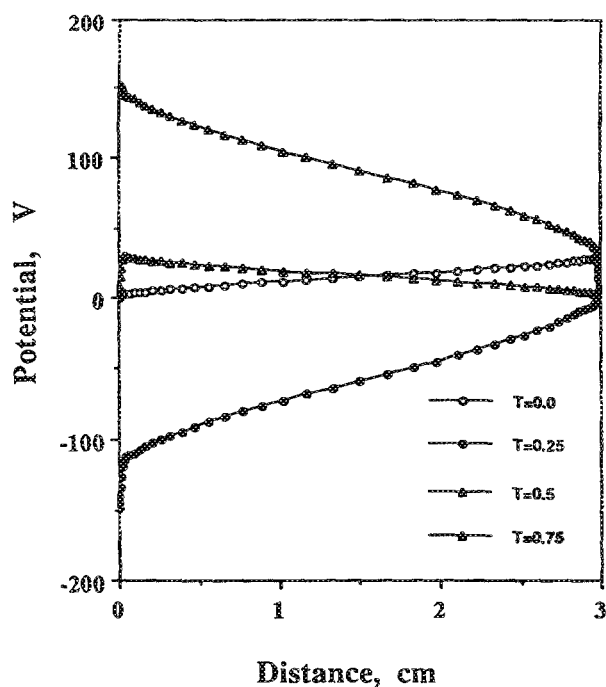


FIG. 10. Spatial and temporal variation of the potential for the electronegative discharge. Conditions were at their basic value.

sheath is much thinner in the electronegative discharge, in accord with experimental observations. This is further seen in Fig. 11, which shows the electric field distribution. The electric field is spatially uniform in the bulk plasma. However, strong electric field gradients are observed in the (thin) sheath. When compared to Fig. 3, one notes much higher electric field strength in the bulk plasma. This is a direct consequence of the large plasma resistance. A high electric field is needed to support the passage of current. Finally, one observes that the electric field undergoes substantial rf modulation in the plasma bulk.

Figure 12 depicts the spatial and temporal electron temperature profiles. The electron temperature is spatially uniform in the bulk, but changes rapidly in the sheath. The bulk electron temperature is seen to undergo severe modulation in time. In fact, the electron temperature is modulated at twice the applied rf frequency. The time-average electron temperature is 2.24 eV in reasonable agreement with a temperature of 2.0 eV calculated by a bulk plasma model under similar conditions.¹² Figure 13 shows the spatial and temporal distribution of the ionization [Fig. 13(a)] and excitation [Fig. 13(b)] rate [see Eq. (29) and (30)]. In contrast to the electropositive discharge, where modulation is limited in the sheath (Fig. 6), severe modulation, at twice the rf frequency, is also seen in the bulk. A peak in excitation and ionization near the plasma-sheath boundary is again observed. The ionization rate as a function of time in the cycle for different positions in the discharge is illustrated in Fig. 14(a). The corresponding excitation rate is shown in Fig. 14(b). The severe modulation is clearly observed especially in the discharge center (dimensionless position $S = 0.5$). At an excitation frequency of 10 MHz the tail of the electron energy distribution function (EEDF) can respond to the variations

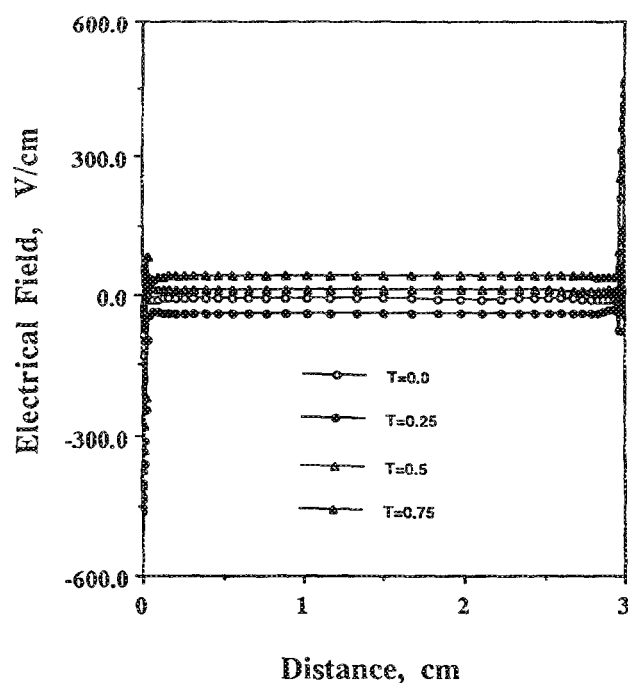


FIG. 11. Spatial and temporal variation of the electric field for the electronegative discharge. Conditions were at their basic value.

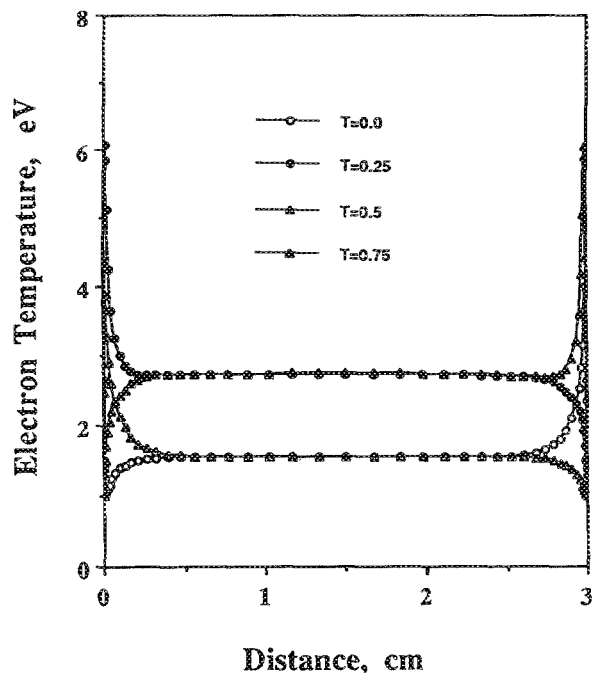


FIG. 12. Spatial and temporal variation of the electron temperature for the electronegative discharge. Conditions were at their basic value.

of the field (this depends on the electron energy-exchange frequency (see Ref. 10). As the electric field reverses direction during the cycle, the electric field crosses zero. As this happens the EEDF cools down, and ionization as well as plasma emission are quenched. One further observes that, near the electrode (at $S = 0.0648$), both ionization and emission peak around the time when the electrode voltage has its maximum negative value (at $T = 0.25$). However, in the discharge center (at $S = 0.5$), the two peaks during the cycle are of equal strength due to symmetry. The qualitative

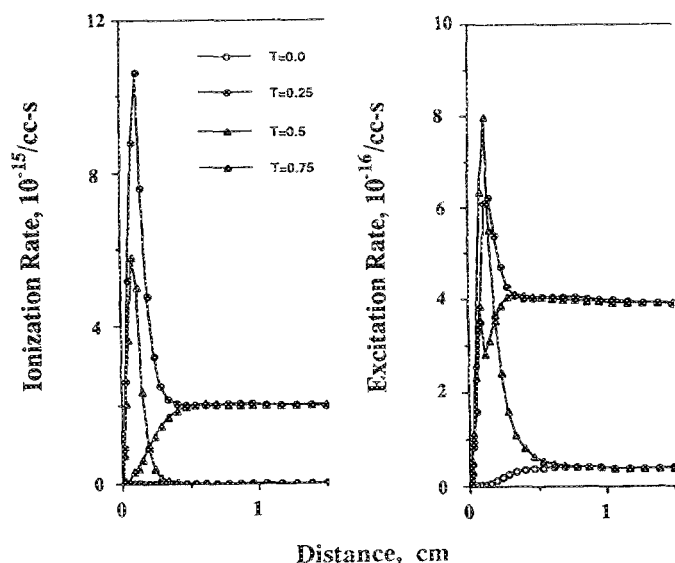


FIG. 13. Spatial and temporal variation of the ionization rate and excitation rate for the electronegative discharge. Conditions were at their basic value.

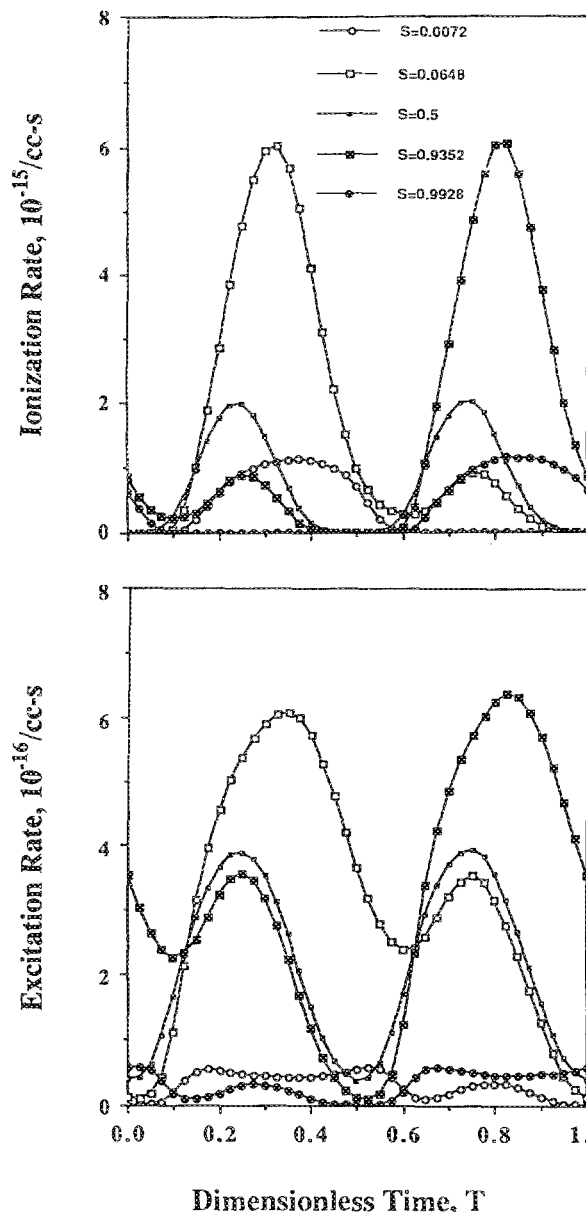


FIG. 14. Temporal variation of the ionization rate and excitation rate at different positions in the gap for the electronegative discharge. Conditions were at their basic value.

features of plasma emission modulation in the discharge center shown in Fig. 14 were observed experimentally by Donnelly *et al.*¹¹ in a chlorine discharge. Temporally resolved plasma emission from SF_6 discharges was studied by Gogolides *et al.*⁸ The spatial and temporal variations in plasma emission are shown pictorially in the 3-D plot of Fig. 15. The strong emission modulation at twice the rf frequency is clear.

The chlorine discharge was also studied for a frequency of 100 MHz keeping the other operating conditions at their basic value (0.5 Torr pressure and 150 V peak voltage). The time-average particle density profiles in the gap are shown in Fig. 16. The electron density is much higher compared to the 10 MHz discharge (compare to Fig. 9). Such increase in electron density with increasing frequency (keeping the peak voltage constant) was also found in the electropositive discharge. Since the electron density is rather high, the nega-

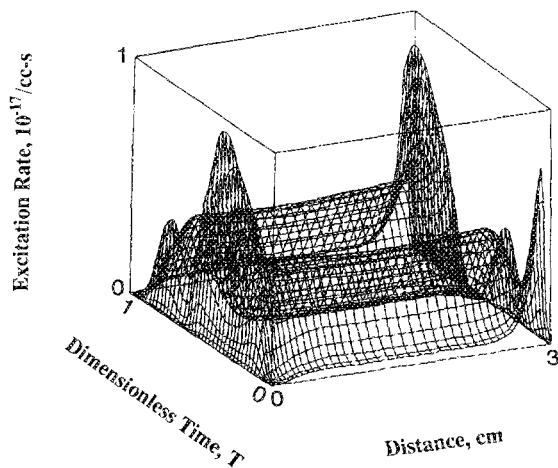


FIG. 15. Spatial and temporal variation of the excitation rate for the electronegative discharge. Conditions were at their basic value.

tive ion density is now smaller than the positive ion density, such that quasineutrality exists in the bulk plasma. One further notes that the plasma sheath is thinner compared to the 10 MHz case. The corresponding excitation rate as a function of time in the discharge is shown in Fig. 17. The modulation is not as severe as in the 10 MHz case. At the excitation frequency of 100 MHz the electron energy-exchange frequency becomes comparable to the excitation frequency. Hence, the EEDF is not allowed enough time to relax completely, as the electric field crosses zero. This is especially evident in the excitation profile (compare to Fig. 14 in which nearly complete modulation is evident).

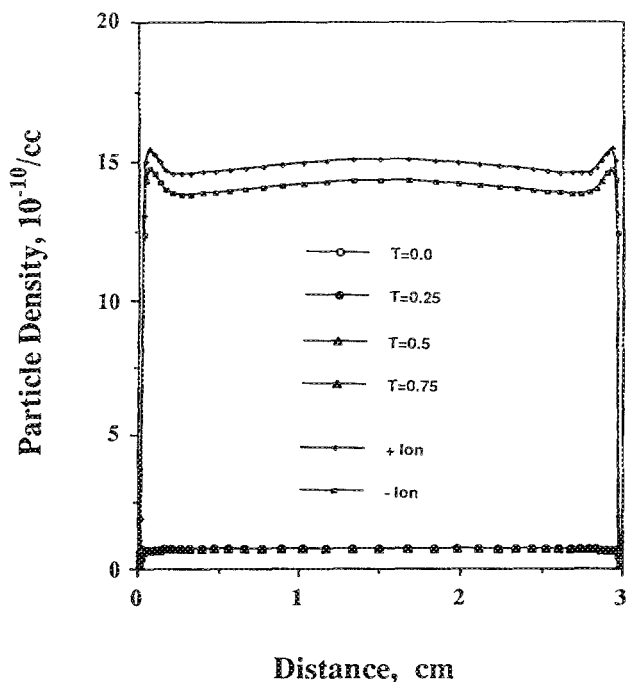


FIG. 16. Spatial and temporal variation of electron, positive ion, and negative ion density for the electronegative discharge. Conditions were at their basic value, except that the frequency was 100 MHz.

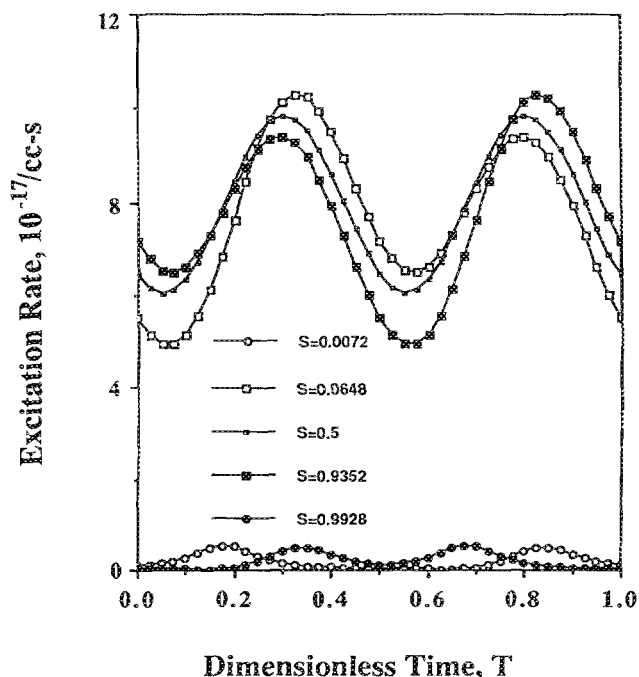


FIG. 17. Temporal variation of the excitation rate at different positions in the gap for the electronegative discharge. Conditions were at their basic value, except that the frequency was 100 MHz.

V. SUMMARY AND CONCLUDING REMARKS

A continuum model was used to analyze charged particle transport and potential distribution in low pressure radio frequency (rf) discharges. The method of lines with orthogonal collocation on finite elements for the spatial discretization was found to be an effective numerical technique for solving the stiff system of partial differential equations describing the model. An argonlike discharge was examined as an example of an electropositive discharge. Cases of varying the applied voltage and the excitation frequency were shown. A discharge in pure chlorine was studied as an example of an electronegative discharge. The main features of the two kinds of discharges were compared with one another.

In the chlorine discharge, the electron density was two orders of magnitude lower than the negative ion density. The low electron density resulted in large potential drop across the bulk plasma and comparatively high bulk electric fields. The electron temperature, ionization rate, and excitation rate were strongly modulated by the rf in the bulk. All of the above features were not observed in the argonlike discharge. In addition, the plasma sheath was much thinner in the chlorine discharge. The electron temperature and excitation profiles in the bulk plasma agreed qualitatively with experimental observations.

The results presented in this study show that continuum models can capture all the main features observed in both electropositive and electronegative glow discharges. However, the range of applicability of these models is limited to the relatively high pressure regime, and to operating conditions for which beam electrons do not play an important role.

Detailed comparison with experimental observations is needed to determine the degree of complexity which needs to be incorporated into the glow discharge models. For example, only one electron excitation reaction, and constant particle diffusivity and mobility were used in the present work. In addition, the presence of Cl atoms resulting from Cl₂ dissociation was neglected. The experimentally verified glow discharge models may then be combined with the rather well-developed neutral transport and reaction models. The result could be a powerful tool for the design and analysis of plasma reactors.

ACKNOWLEDGMENTS

We are grateful to the National Science Foundation (CBT 8708908), to Texas Instruments, and to the Welch Foundation for financial support. Thanks are due to the Houston Advanced Research Center (HARC) for providing an NEC SX-2 supercomputer-time grant. S.-K. Park was partially supported by a scholarship from the Ministry of Education, Republic of Korea.

¹D. M. Manos and D. L. Flamm, Eds., *Plasma Etching: An Introduction* (Academic, New York, 1990).

²R. W. Boswell and I. J. Morey, *Appl. Phys. Lett.* **52**, 21 (1988).

³D. B. Graves and K. F. Jensen, *IEEE Trans. Plasma Sci.* **PS-14**, 78 (1986).

⁴D. B. Graves, *J. Appl. Phys.* **62**, 88 (1987).

⁵A. D. Richards, B. E. Thompson, and H. H. Sawin, *Appl. Phys. Lett.* **50**, 492 (1987).

⁶M. S. Barnes, T. J. Cotler, and M. E. Elta, *J. Comput. Phys.* **77**, 53 (1988).

⁷J.-P. Boeuf, *Phys. Rev. A* **36**, 2782 (1987).

⁸E. Gogolides, J.-P. Nicolai, and H. H. Sawin, *J. Vac. Sci. Technol. A* **7**, 1001 (1989).

⁹S.-K. Park and D. J. Economou, *J. Appl. Phys.* (to be published).

¹⁰G. L. Rogoff, J. M. Kramer, and R. B. Piejak, *IEEE Trans. Plasma Sci.* **PS-14**, 103 (1986).

¹¹V. M. Donnelly, D. L. Flamm, and R. Bruce, *J. Appl. Phys.* **58**, 2135 (1985).

¹²E. S. Aydil, Ph.D. Thesis (in progress), University of Houston.

¹³L. Lapidus and W. E. Schiesser, *Numerical Methods for Differential Systems* (Academic, New York, 1976).

¹⁴B. A. Finlayson, *Nonlinear Analysis in Chemical Engineering* (McGraw-Hill, New York, 1980).

¹⁵M. E. Davis, *Numerical Methods and Modeling for Chemical Engineers* (Wiley, New York, 1984).

¹⁶C. deBoor, *SIAM J. Numer. Anal.* **14**, 441 (1977).

¹⁷C. deBoor, *A Practical Guide to Splines* (Springer, New York, 1978).

¹⁸A. C. Hindmarsh, in *Advances in Computer Methods for Partial Differential Equations IV*, edited by R. Vichnevetsky and R. S. Stepleman (IMACS, North Holland, 1981), p. 312.

¹⁹A. C. Hindmarsh, in *Scientific Computing*, edited by R. S. Stepleman *et al.* (IMACS, North Holland, 1983), p. 55.

²⁰A. C. Hindmarsh, Lawrence Livermore Lab. Report UCRL-87406 (1982) and UCRL-89311 (1983).

²¹B. Chapman, *Glow Discharge Processes: Sputtering and Plasma Etching* (Wiley, New York, 1980).

²²Y.-H. Oh, N.-H. Choi, and D.-I. Choi, *J. Appl. Phys.* **67**, 3264 (1990).

²³G. S. Selwyn, L. D. Baston, and H. H. Sawin, *Appl. Phys. Lett.* **51**, 898 (1987).

²⁴G. L. Rogoff, *J. Phys. D* **18**, 1533 (1985).